References and Notes

1. G. Robles-De-La-Torre, V. Hayward, *Nature* **412**, 445 (2001).
2. S. Matsumoto *et al.*, *Surg. Endosc. Ultrasound Intervent. Tech.* **11**, 939 (1997).
3. N. Sakai, M. Tatsuta, H. Yano, H. Iishi, S. Ishiguro, *Gastrointest. Endosc.* **51**, 69 (2000).
4. O. Tohyama, S. Maeda, H. Itoh, *IEEE J. Sel. Top. Quant. Electron.* **5**, 115 (1999).
5. P. K. Plinkert, I. Baumann, E. Flemming, *Laryngorhinootologie* **76**, 543 (1997).
6. P. N. Brett, R. S. Stone, *Proc. Inst. Mech. Eng. [H.]* **211**, 309 (1997).
7. The tactile signal may be displayed on a monitor as a digital hardness score (*2*), or a virtual reality tool similar to the NanoManipulator (*37*) may be developed. In the NanoManipulator, the force from the manipulator performing nanoscale displacement of molecules is transmitted to a joy stick, giving the operator a "touch sensation" during the manipulation.
8. P. Dario, E. Guglielmelli, C. Laschi, *J. Robot. Syst.* **18**, 673 (2001).
9. Y. Okumura *et al.*, *Adv. Robot.* **18**, 699 (2004).
10. Y. B. Jia, *IEEE Trans. Robot.* **21**, 726 (2005).
11. M. Kaneko, K. Tanie, *IEEE Trans. Rob. Autom.* **10**, 355 (1994).
12. A. M. Okamura, M. R. Cutkosky, *Int. J. Robot. Res.* **20**, 925 (2001).
13. R. Tajima, S. Kagami, M. Inaba, H. Inoue, *Adv. Robot.* **16**, 381 (2002).
14. M. Shikida, T. Shimitzu, K. Sato, K. Itoigawa, *Sens. Actuators A Phys.* **103**, 213 (2003).
15. J. Engel, J. Chen, C. Liu, *J. Micromech. Microeng.* **13**, 359 (2003).
16. R. D. Howe, M. R. Cutkosky, *IEEE Trans. Rob. Autom.* **9**, 140 (1993).
17. D. De Rossi, F. Carpi, E. P. Scilingo, *Adv. Colloid Interface Sci.* **116**, 165 (2005).
18. C. Domenici, D. Derossi, *Sens. Actuators A Phys.* **31**, 97 (1992).
19. S. P. Lacour, C. Tsay, S. Wagner, *IEEE Electron Device Lett.* **25**, 792 (2004).
20. T. Someya *et al.*, *Proc. Natl. Acad. Sci. U.S.A.* **101**, 9966 (2004).
21. N. J. Ferrier, R. W. Brockett, *Int. J. Robot. Res.* **19**, 795 (2000).
22. B. L. Gray, R. S. Fearing, *IEEE Int. Conf. Robot. Autom.* **1**, 1 (1996).
23. J. W. Morley, A. W. Goodwin, I. Darian-Smith, *Exp. Brain Res.* **49**, 291 (1983).
24. R. S. Johansson, R. H. LaMotte, *Somatosens. Res.* **1**, 21 (1983).
25. As a finger touches a surface, the fingernail color begins to redden above a threshold force of ~0.3 N and completely reddens at ~1 N. For ordinary grabbing and sensing operations, the force at the fingertip ranges from 1 to 4 N. Assuming a contact area of ~1 cm^2, a reasonable threshold stress to determine texture by human finger would be in the 10 to 40 kPa range (*38*).
26. G. Decher, *Science* **277**, 1232 (1997).
27. C. Y. Jiang, S. Markutsya, Y. Pikus, V. V. Tsukruk, *Nat. Mater.* **3**, 721 (2004).
28. Alternating monolayers of Au (10 nm) and CdS (3 to 4 nm) nanoparticles (NP), spaced by a dielectric layer (DL) composed of PSS and PAH, are deposited using a layer-by-layer assembly process by sequentially dipping (*26*) in four solutions: The 0.1% (by weight) solutions of PSS and PAH of molecular weights 70 and 15 kD have a pH of 8 and 4.2, respectively. The anionic Au and CdS deposition solutions with 10^{12} and 10^{16} particles/ml have a pH of 6 and 4.5, respectively. The deposition time for the polymer monolayer is 30 min each; for the Au and cationic CdS nanoparticles, it is 24 hours and 1 hour, respectively. All the solutions are in DI water (filtered through 20 μ Millipore filter), and each deposition step is followed by a rigorous wash in DI. The chemical structure of DL between Au and CdS nanoparticle monolayers is Au(NP)/PAH/$(PSS/PAH)_3$/PSS/CdS(NP). The process is initiated by cleaning the 1-inch by 1-inch ITO-coated (400 nm) glass surface in piranha solution (H_2SO_4/H_2O_2; 3:1 by volume) to make the electrode surface negatively charged. The final structure of the device is glass/ITO/DL/$[Au\text{-}NP/DL/CdS\text{-}NP/DL]_2$ /Au-NP/DL/Au-electrode/plastic. The structure of the flexible electrode is Au (200 nm)/Cr (70 nm)/Al (12 μm)/siloxane rubber (~5 μm). The Au is sputter-deposited on the Al foil with Cr as the adhesion layer. Poly(dimethyl siloxane) is spincast on the other side for the electrode, followed by UV cross-linking. The resultant free-standing electrode is physically placed on the device with the Au side in physical contact with the device surface.
29. R. H. Fowler, L. Nordheim, *Proc. R. Soc. London A* **119**, 173 (1928).
30. T. Cassagneau, T. E. Mallouk, J. H. Fendler, *J. Am. Chem. Soc.* **120**, 7848 (1998).
31. J. Y. Ouyang, C. W. Chu, C. R. Szmanda, L. P. Ma, Y. Yang, *Nat. Mater.* **3**, 918 (2004).
32. S. O. Kasap, in *Principles of Electrical Engineering Materials and Devices, Revised Edition*, S. O. Kasap, Ed. (McGraw Hill, New York, 2000), pp. 284–288.
33. D. M. DeLongchamp, P. T. Hammond, *Chem. Mater.* **15**, 1165 (2003).
34. M. F. Durstock, M. F. Rubner, *Langmuir* **17**, 7865 (2001).
35. K. L. Johnson, *Contact Mechanics* (Cambridge Univ. Press, Cambridge, 1985).
36. Recently, 20-μm device features have been demonstrated on flexible circuits (*39*).
37. A. Seeger *et al.*, *J. Vac. Sci. Technol. B* **19**, 2717 (2001).
38. S. A. Mascaro, H. H. Asada, *IEEE Trans. Robot. Autom.* **17**, 698 (2001).
39. T. W. Kelley *et al.*, *Chem. Mater.* **16**, 4413 (2004).
40. We thank the Office of Naval Research (N00014-01-1-0977) and the National Science Foundation (534812) for financial support.

14 February 2006; accepted 7 April 2006
10.1126/science.1126216

Converting Ceria Polyhedral Nanoparticles into Single-Crystal Nanospheres

Xiangdong Feng,[1]*† Dean C. Sayle,[2] Zhong Lin Wang,[3,4,5]* M. Sharon Paras,[6] Brian Santora,[1] Anthony C. Sutorik,[6] Thi X. T. Sayle,[2] Yi Yang,[1] Yong Ding,[3] Xudong Wang,[3] Yie-Shein Her[1]

Ceria nanoparticles are one of the key abrasive materials for chemical-mechanical planarization of advanced integrated circuits. However, ceria nanoparticles synthesized by existing techniques are irregularly faceted, and they scratch the silicon wafers and increase defect concentrations. We developed an approach for large-scale synthesis of single-crystal ceria nanospheres that can reduce the polishing defects by 80% and increase the silica removal rate by 50%, facilitating precise and reliable mass-manufacturing of chips for nanoelectronics. We doped the ceria system with titanium, using flame temperatures that facilitate crystallization of the ceria yet retain the titania in a molten state. In conjunction with molecular dynamics simulation, we show that under these conditions, the inner ceria core evolves in a single-crystal spherical shape without faceting, because throughout the crystallization it is completely encapsulated by a molten 1- to 2-nanometer shell of titania that, in liquid state, minimizes the surface energy. The principle demonstrated here could be applied to other oxide systems.

For large-scale, wafer-level fabrication of nanodevices and their integration with silicon technology, the surface of a wafer needs to be perfectly flat (on the order of less than 2 to 4 nm) and free from defects. Ceria nanoparticles are a key abrasive nanomaterial for chemical-mechanical planarization (CMP) of advanced integrated circuits. CMP using nanoparticles accounted for 60% of the $1 billion market for nanomaterials in 2005 (*1*, *2*). As the size of the integrated circuit architecture decreases for chip miniaturization and nanorization, defects must be reduced by at least 50% to make chip mass-manufacturing viable for each generation.

Crystalline ceria nanoparticles have been synthesized by means of a variety of methods, including room temperature solution precipitation (*3*, *4*), microwave-assisted hydrothermal route (*5*), hydrothermal crystallization (*6*), microemulsion (*7*), mechanochemical processing (*8*), thermal decomposition (*9*), aerosol pyrolysis (*10*, *11*), sol-gel method (*12*), thermal hydrolysis (*13*), and solvothermal synthesis (*14*). But ceria nanoparticles synthesized by these techniques are faceted and possess sharp edges, corners, and apexes (*15*, *16*), which are more prone to scratch the silicon wafers and limit the CMP rates. For superior performance, spherical nanoparticles would be ideal because they can act like ball bearings and can polish the silicon surface without scratching it. However, this is a challenge because spherical single-crystal nanoparticles must have energetically unfavorable high-index surfaces.

We produced nanospheres of CeO_2 and $Ce_{1-x}Ti_xO_2$ ($0 \leq x \leq 0.25$) with a liquid-phase flame spray pyrolysis of solutions of cerium and titanium precursors dissolved in a flammable solvent (i.e., an alcohol) (*17*, *18*) (fig. S1). The alcohol solution of metal precursors is pumped at a rate of 150 g/min into an atomization device that sprays a fine mist into the combustion chamber. The mist is directly ignited by pilot torches in the line of the spray, leading to instantaneous combustion of the metal precur-

sors and generation of the desired metal oxide as a nanoparticulate "smoke." Depending on experimental conditions, combustion occurs in the range of 1200° to 2500°C. Temperatures are rapidly quenched downstream from the initial combustion zone, leading to a measure of kinetic control over the chemical reaction, crystallization, phase evolution, and particle growth. Due to the short particle residence time, atomic diffusion and particle growth end rapidly after initial particle formation. The product stream (powder plus CO_2 and water vapor) is drawn from the combustion chamber by exhaust fans into powder collectors. The apparatus used for this study can generate nanoparticles at a rate as high as about 300 g/hour.

Pure ceria nanoparticles without doping were synthesized through liquid-phase flame spray pyrolysis of a solution made from dissolving cerium carbonate into propionic acid (*19*). The nondoped CeO_2 nanoparticles show faceted and occasionally irregular shapes (Fig. 1A), and have a large size variation. Transmission electron microscopy (TEM) images show that each nanoparticle is a single crystal (Fig. 1B). Electron diffraction patterns acquired from dozens of nanoparticles indicate that they are cubic ceria phase with the fluorite (CaF_2)–type structure (Fig. 1C). High-resolution TEM clearly shows that the nanoparticles are dominated by {111} and {001} type of facets and some of them exhibit octahedral and truncated octahedral shape (Fig. 1D). For cubic structured ceria, {111} and {001} are the dominant facets, possibly resulting from low surface energy. The surfaces of the nanoparticles are atomically sharp, abrupt, and clean without visible contaminant (fig. S2). In comparison to image simulation, the (001) surface is likely terminated with oxygen (see the simulated image in fig. S2).

Ceria nanospheres doped with varied amounts of titanium were synthesized through liquid-phase flame spray pyrolysis (L-FSP) of a solution made by dissolving cerium carbonate into propionic acid with stoichiometric amounts of titanium (IV) (triethanolaminato) isopropoxide (*20*). The cerium oxide containing 6.25 atomic % of Ti is dominated by spherical shapes (Fig. 1E and fig. S3), and each particle is a single crystal (Fig. 1F). High-resolution TEM shows that each particle is a single crystal with visible {111}, {001}, and high-index facets (Fig. 1G and figs. S4 to S6), and the particle shape is close to being an ideal sphere. The smaller size particles are single crystals and more spherical (Fig. 1H). For larger size nanospheres, the facets are a little more pronounced, and {110} facets can also be identified (Fig. 1I). The crystal lattice extends to the surface of the nanosphere and the surfaces are fairly clean and atomically sharp.

For the ceria nanosphere doped with 12.5 atomic % Ti, the particles are dominated by spherical shape and single crystals (Fig. 2A). High-resolution TEM clearly shows that a large particle is nearly spherical and its surface is covered with a uniform amorphous thin layer (1 to 2 nm) (Fig. 2B). The area of the {111} and {001} facets are largely reduced with an increased formation of high-index planes, conditions required for forming a spherical shape. The characteristics displayed by a smaller size particle are similar to those of the bigger ones (Fig. 2C). Nanospheres of different sizes can be separated by a centrifugal (fig. S7).

To identify the nature of the surface amorphous layer, chemical maps of Ce and Ti were acquired for the 12.5 atomic % Ti–doped nanospheres with the use of a scanning TEM (STEM) with a probe size of ~1 nm. The morphology and distribution of the nanospheres is displayed in the bright-field STEM image (Fig. 2D), and corresponding maps for Ce and Ti acquired with the use of the x-ray signal emitted from the sample as the probe was scanned across the sample are shown in Fig. 2, E and F, respectively. Ti atoms are distributed at the surface of the particles, and some TiO_2 particles were also found. The data show that the surface amorphous layer is TiO_2.

We performed molecular dynamics (MD) simulations using the DL_POLY code (*21*) and potential parameters taken from (*22*, *23*) to understand the formation process of the nanospheres. Most atomistic simulations start by proposing a structural model; however, this has the disadvantage of requiring the simulator to choose or design a potentially erroneously structural model. Our strategy involved the simulation of crystallizing nanoparticles in flame by constructing an amorphous/molten precursor that was then crystallized at high temperatures and quenched to room temperature.

At the beginning of the simulation, two identical "cubes" of CeO_2, comprising 15,972 atoms (5324 Ce and 10,648 O), were generated. One cube was doped with 25 atomic % Ti (1330 substitution atoms, located at the surface), whereas the other nanoparticle remained "pure." Both cubes were first amorphosized

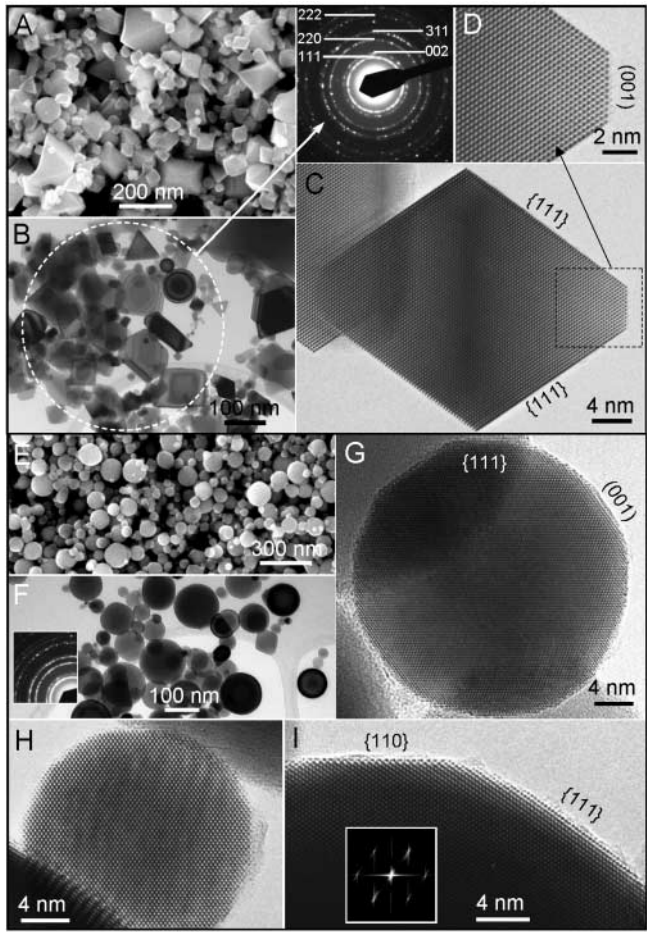

Fig. 1. (**A** to **D**) Microstructure of CeO_2 nanoparticles without Ti doping. (A) Scanning electron microscopy (SEM) image, (B) low-magnification TEM image, and [(C) and (D)] high-resolution TEM images of the ceria nanocrystals with faceted shapes. The inset between (A) and (D) is an electron diffraction pattern from the area circled in (B). (**E** to **I**) Microstructure of CeO_2 nanospheres doped with 6 atomic % of Ti. (E) SEM image, (F) low-magnification TEM image, and [(G) to (I)] high-resolution TEM images of the ceria nanocrystals, showing their spherical shape and single-crystal structure. The inset in (F) is an electron diffraction pattern recorded from the area, showing the cubic ceria structure of the sample. The inset in (I) is a fast Fourier transform of the high-resolution TEM image.

[1]Ferro Corporation, 7500 East Pleasant Vally Road, Independence, OH 44131, USA. [2]Cranfield University, Defense Academy of the United Kingdom, Shrivenham, Swindon SN6 8LA, UK. [3]School of Materials Science and Engineering, Georgia Institute of Technology, Atlanta, GA 30332–0245, USA. [4]Department of Advanced Materials and Nanotechnology, College of Engineering, Peking University, 100871 Beijing, China. [5]National Center for Nanoscience and Technology, Beijing 100080, China. [6]Nanocerox, Inc., 712 State Circle, Ann Arbor, MI 48108, USA.

*To whom correspondence should be addressed. E-mail: shawn.feng@jhresearchusa.com (X.D.F.); zhong.wang@mse.gatech.edu (Z.L.W.)

†Present address: James Hardie Building Products, 10901 Elm Avenue, Fontana, CA 92337, USA.

and then recrystallized at high temperature during the simulation. Further simulation details can be found in (*24*, *25*).

Figure 3A shows a series of images for the cooling of the Ti-doped particle. Figure 3, B to H, shows the (room temperature) structure of the nanoparticles at the end of the simulations. The undoped nanoparticle has an octahedral shape and morphology with {111} surfaces, truncated with {100} facets, and includes sharp edges and corners. Conversely, the Ti-doped CeO_2 nanoparticle is effectively spherical. Both structures are in accord with our experimentally synthesized nanoparticles (Figs. 1 and 2).

The crystallization process, starting from the amorphous precursor to the final crystalline structure, was then studied by analyzing a movie of the crystallization simulations. In the undoped system, a single, fluorite-structured (CaF_2), crystalline "seed" was observed to evolve "naturally" within the amorphous sea of ions (Ce and O) during the MD simulation. Ce and O surrounding this seed then started to condense onto its surface, propagating the crystallization front, which traverses through the nanoparticle. Moreover, as the crystallization front impinged the surface, the crystallization was observed to evolve energetically stable {111} surfaces, resulting in a fluorite-structured single crystal of CeO_2 with {111} and {100} facets (Fig. 3, B to D). The simulations also revealed that energy was liberated during this process, which reflects the latent heat of crystallization.

Similar to the undoped CeO_2 nanoparticle, the Ti-doped system also evolved a fluorite-structured crystalline seed (Fig. 3A), and the amorphous sea of ions (Ti, Ce, and O) started to condense onto its surface. The amorphous layer has a short-range ordering but lacks a long-range ordering (figs. S8 and S9). The crystallization front traversed through the nanoparticle emanating spherically from the crystalline seed (Fig. 3A) and continued until it consumed the entire CeO_2 core. As the crystallization front impinged on the outer surfaces of the CeO_2, it did not start to evolve {111} and {100} because it was enveloped by the amorphous TiO_2 shell. Moreover, as the crystallization front moves out to the surface (TiO_2 region), the TiO_2 does not crystallize; rather, it remains amorphous. This enables the nanoparticle to retain its sphericity, which is driven by the system minimizing its surface energy to facilitate an energetically more stable nanoparticle. This is in contrast to the faceted surfaces, including sharp edges and corners, associated with the undoped CeO_2 nanoparticles.

Our synthetic strategy of generating the nanoparticles in flame at about 2500°C facilitates the crystallization of the cerium oxide (CeO_2, melting point 2400°C), while maintaining the TiO_2 in a molten state (TiO_2 melting point 1843°C). In particular, the CeO_2 occupies the core region of the nanoparticle and is encapsulated by a TiO_2 shell; limited Ti(IV) is incorporated into the lattice. Here, in contrast to the undoped CeO_2 system, the CeO_2 core crystallizes while enveloped by a TiO_2 shell. Crucially, because the CeO_2 surfaces are covered with amorphous TiO_2 as they evolve, the energy difference between different surfaces is no longer notable. Therefore, it is the flame

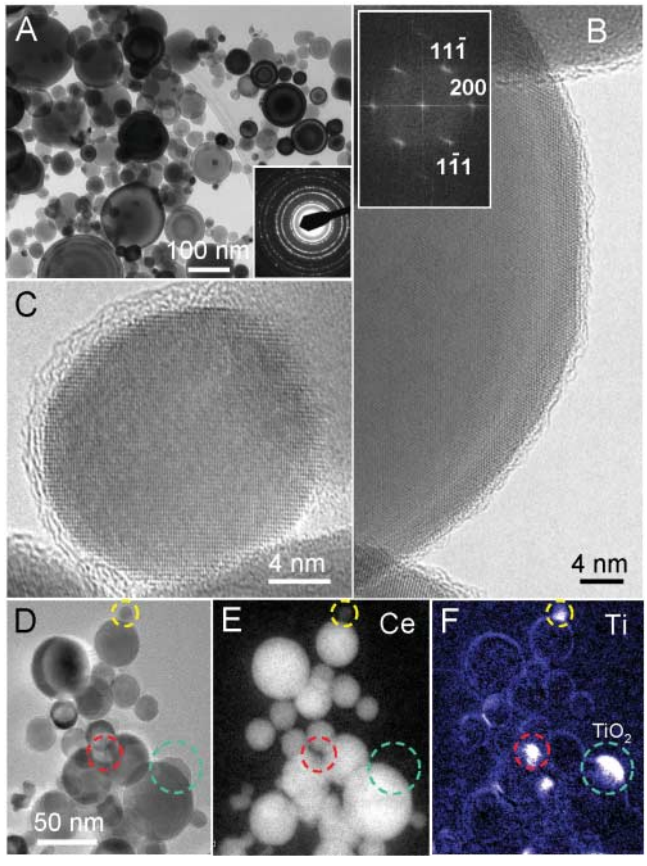

Fig. 2. Microstructure of CeO_2 nanospheres doped with 12 atomic % of Ti. (**A**) Low-magnification TEM image and (**B** and **C**) high-resolution TEM images of the ceria nanocrystals, showing their spherical shape and single-crystal structure as well as the amorphous layer on the surface. The inset in (A) is an electron diffraction pattern recorded from the area, proving the cubic ceria structure of the sample. (**D** to **F**) STEM images of the nanocrystals doped with 12 atomic % of Ti, showing the morphology, corresponding Ce distribution map, and Ti distribution map. The nanospheres are dominated by Ce, and the Ti is distributed at the surfaces. The bright clusters seen in (F) are precipitated TiO_2 particles. The yellow, red, and green circles represent three corresponding particles that are rich in Ti.

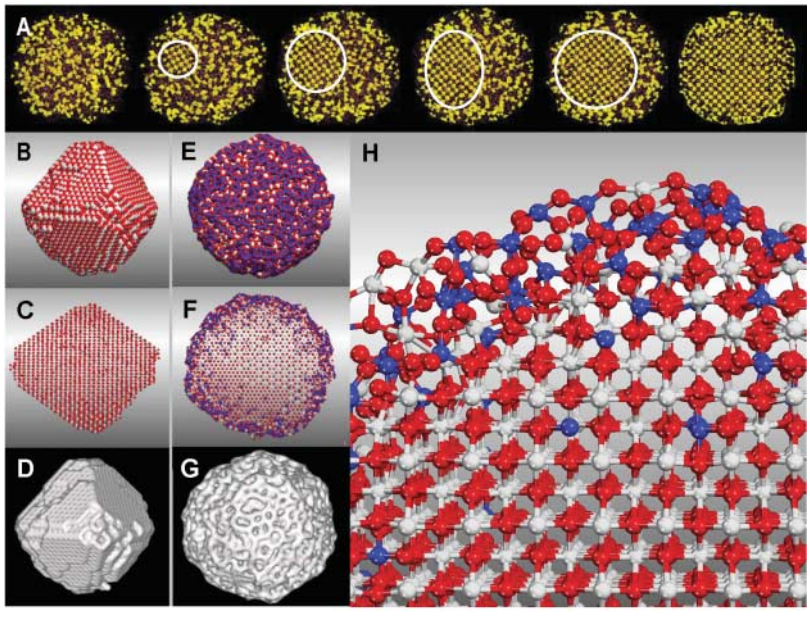

Fig. 3. (**A**) Images taken during a crystallization simulation (Ti-doped CeO_2), showing the initial amorphous precursor (left), evolution, and growth of the seed (circled) to the fully crystalline nanoparticle with amorphous shell (right). (**B** to **D**) Nondoped nanoparticle. (**E** to **G**) Ti-doped CeO_2 nanosphere. (**H**) Enlarged segment of the Ti-doped nanosphere. [(B) and (E)] Sphere model representation of the atom positions. [(C) and (F)] Side view with smaller spheres to view through the nanoparticle. [(D) and (G)] Surface rendered model. Cerium is colored white; Ti(IV) is blue, and oxygen is red. The nanoparticles are about 7 to 8 nm in diameter. All images show actual atom positions and are not schematics.

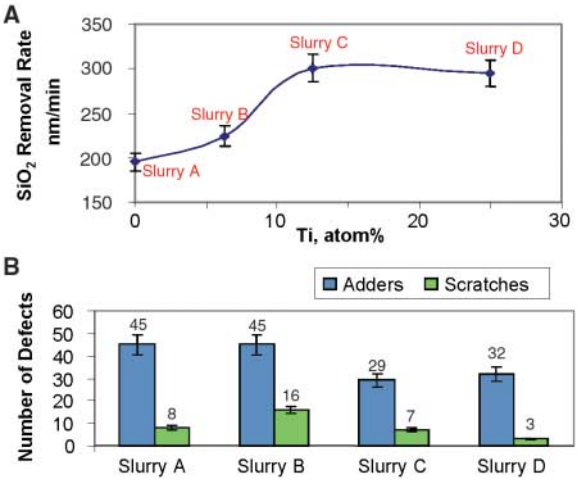

Fig. 4. Chemical-mechanical planarization performance of single-crystal nanospheres of $Ce_{1-x}Ti_xO_2$, ($x = 0 - 0.25$). (**A**) A comparison of the thermal oxide, SiO_2, removal rates among the four CMP slurries. (**B**) A comparison of the defect rates in terms of the total number of the adders that adhere to the pattern wafers after CMP testing and the number of scratches observed. Error bars show means ± SD.

temperature that facilitates spherication of the Ti-doped CeO_2 nanoparticles.

The $Ce_{1-x}Ti_xO_2$ ($0 \leq x \leq 0.25$) nanospheres can be used as an abrasive material for CMP of advanced integrated circuits because of its special spherical and crystalline structure characteristics. The primary function of CMP is to smooth a nominally macroscopically flat wafer at the feature (or microlevel), i.e., planarize features. Therefore, two of the important parameters to evaluate a CMP slurry are the uniform material removal rate across the wafer and the defect concentration of the wafer. Cerium oxide particles have been used in the oxide or silicon wafer polishing because of its selectivity and good oxide-removal rate. The cerium oxide particles have always been crystalline and cubic in structure. It is believed that the relatively sharp edges of the cubic-shaped ceria particles (Fig. 1) may gouge and/or scratch wafer surfaces that are being planarized.

Four CMP slurries were prepared by mixing 1.0 weight % of the spherical single-crystalline $Ce_{1-x}Ti_xO_2$ powders (as synthesized without any particle-size separation) with a chemical additive, proline (table S1) (*26*). The CMP efficiency is characterized by the removal rate of thermal oxide, SiO_2 (*27*), which is shown in Fig. 4A and table S1. The rate for the undoped CeO_2 nanoparticles of slurry A is 195 nm/min. The SiO_2 removal rates gradually increased to 224 and 301 nm/min as the Ti content in the nanoparticles $Ce_{1-x}Ti_xO_2$ increased to $x = 0.0625$ and 0.125, respectively. The CMP rate decreased back to 295 nm/min as the Ti content further increased to $Ce_{0.75}Ti_{0.25}O_2$.

The defects generated during CMP are detrimental to the chip production yield, and in the production of advanced integrated circuits the CMP process is used many times. Each successive generation of advanced chips requires at least a 50% reduction in defect rate in order to make the chip mass-manufacturing viable in accommodating the reduced feature sizes and increased number of interconnects in each chip. The adders and, more importantly, the scratches are substantially reduced as the nanoparticles become more spherical and contain higher Ti contents (Fig. 4B). This can be easily understood in terms of the lack of sharp edges and corners as well as the ability to roll freely on the wafer surface during polishing as the nanoparticles become more spherical.

We report the synthesis of spherical, single-crystal, Ti-doped CeO_2 nanoparticles at large scale (up to 300 g/hour). This was achieved by synthesizing Ti-doped CeO_2 nanoparticles in flame temperatures that facilitate crystallization of the CeO_2 yet retain the TiO_2 in a molten state. The (molten) titanium oxide shell encapsulates the inner ceria core and accommodates a spherical morphology, which minimizes its surface energy, and the nanoparticles become more perfect (spherical) with increasing TiO_2 content. For CMP, spherical, single-crystal Ti-doped CeO_2 nanoparticles are shown to facilitate an 80% reduction in defects and a 50% increase in the silica removal rate. This technology will impact the development of high-quality and high-precision microelectronics and nanoelectronics over large-size wafers. The methodology demonstrated here for synthesizing spherical single-crystal inorganic particles might offer unlimited possibilities in a broad range of fields such as chemical mechanical planarization, photonics, magnetics, catalysis, and inorganic pigment where spherical nanoscale inorganic particles are pivotal.

References and Notes

1. R. K. Singh, R. Bajaj, *Mater. Res. Soc. Bull.* **27**, 743 (2002).
2. CMP is a process that is used in the semiconductor industry to isolate and connect individual transistors on a chip. The CMP process has been the fastest growing semiconductor operation in the past decade, and its future growth is expected to be equally explosive because of the introduction of copper-based interconnects in advanced microprocessors and other applications of CMP for next-generation nanoscale devices. The CMP slurries typically contain particle-based abrasives, which constituted nearly 60% of the total $1 billion worldwide market for nanopowders in 2005.
3. H. Chen, H. Chang, *Ceram. Int.* **31**, 795 (2005).
4. F. Zhang *et al.*, *Appl. Phys. Lett.* **80**, 127 (2002).
5. F. Bondioli *et al.*, *J. Mater. Chem.* **15**, 1061 (2005).
6. P. Shuk, M. Greenblatt, *Solid State Ionics* **116**, 217 (1999).
7. A. Bumajdad, M. I. Zaki, J. Eastoe, L. Pasupulety, *Langmuir* **20**, 11223 (2004).
8. T. Tsuzuki, J. S. Robinson, P. G. J. McCormick, *J. Australas. Ceram. Soc.* **38**, 15 (2002).
9. Y. Wang, T. Mori, J. Li, T. Ikegami, *J. Am. Ceram. Soc.* **85**, 3105 (2002).
10. E. Lopez-Navarrete, A. Caballero, A. R. Gonzalez-Elipe, M. Ocana, *J. Mater. Res.* **17**, 797 (2002).
11. T. T. Kodas, M. J. Hampden-Smith, *Aerosol Processing of Materials* (Wiley-VCH, New York, 1999).
12. A. Hartridge, A. K. Bhattacharya, *J. Phys. Chem. Solids* **63**, 441 (2002).
13. M. Hirano, Y. Fukuda, H. Iwata, Y. Hotta, M. Inagaki, *J. Am. Ceram. Soc.* **83**, 1287 (2000).
14. S. Yabe *et al.*, *Kidorui* **34**, 124 (1999).
15. Z. L. Wang, X. D. Feng, *J. Phys. Chem. B* **107**, 13563 (2003).
16. F. Zhang, Q. Jin, S.-W. Chan, *J. Appl. Phys.* **95**, 4319 (2004).
17. C. Bickmore, K. Waldner, D. Treadwell, R. M. Laine, *J. Am. Ceram. Soc.* **79**, 1419 (1996).
18. A. C. Sutorik, M. S. Baliat, *Mater. Sci. Forum* **386**, 371 (2002).
19. To prepare a ceria stock solution, 3100 g of Propionic Acid (Food Grade, Univar) was heated in a 12-liter round-bottom flask. Once refluxing, a total of 740 g cerium carbonate (99.9995%, Pacific Industrial Development Corporation) was added. The solution was turbid due to insoluble cerium sources and impurities. Once the solution cooled to room temperature, 620 g of deionized water was added, and the solution was vacuum filtered through a 0.2 μm filter. This stock solution (9 to 10 weight % CeO_2 as determined by mass loss on heating) was then diluted with a mixture of methanol:water (5.2:1 weight ratio) to a final solution of about 5 weight % ceria before flame prolysis. The L-FSP operating parameters are pumping rate at 120 g/min, the atomizer oxygen flow at 3.4 m^3/hour, and supplemental oxygen flow at 7.0 m^3/hour.
20. To prepare titanium-doped ceria, $Ce_{1-x}Ti_xO_2$, with $x =$ 0.0625, 0.125, and 0.25, stoichiometric amounts of titanium (IV) (triethanolaminato) isopropoxide (TYZOR-TE) from Dupont were added to the ceria stock solution prepared above (*23*), and the combined solution was diluted to 4 to 5 weight % oxide with methanol:water (5.2:1 weight ratio). The liquid-phase flame spray pyrolysis operating parameters are the same as (*23*).
21. DL_POLY, W. Smith and T. R. Forester, copyright by the council for the Central Laboratory of the Research Councils, Daresbury Laboratory, Daresbury, Warrington, UK, 1996 (www.cse.clrc.ac.uk/msi/software/DL_POLY/).
22. T. X. T. Sayle, S. C. Parker, C. R. A. Catlow, *Surf. Sci.* **316**, 329 (1994).
23. D. C. Sayle, C. R. A. Catlow, M. A. Perrin, P. Nortier, *J. Phys. Chem. Solids* **56**, 799 (1995).
24. T. X. T. Sayle, S. C. Parker, D. C. Sayle, *Chem. Commun.* **21**, 2438 (2004).
25. For the Ti-doped nanoparticle, constant volume MD simulation was performed for 7000 ps at 3750 K. The nanoparticle was then quenched: MD simulation was performed for 400 ps at 273 K. Each simulation required about 100 hours with the use of 96 processors of a SunFire Galaxy–class supercomputer.
26. W. G. America, S. V. Babu, *Electrochem. Solid-State Lett.* **7**, G327 (2004).
27. The SiO_2 film layer for CMP testing was a 1000-nm thermal oxide film on a silicon wafer (of size 200 mm). The wafers were polished with the use of a Strasbaugh 6EC polisher, a Rodel IC1000 pad with Suba IV backing at a down pressure of 3164 kg/m^2, and a table and head rotation speed of 130 rpm, and slurry flow rate of 150 ml/min. The defect study was performed on patterned Massachusetts Institute of Technology–mask silica wafers by polishing the wafer for 60 s using the above mentioned polishing conditions. The defects were examined under an Applied Materials WF736 defect inspection station. The polishing slurry mixture was adjusted to pH 4 with the use of nitric acid and was then subjected to high-shear mixing for 30 min before polishing. The defect was examined by optical detection techniques. A laser beam illuminated the surface, and the surface roughness was retrieved from the reflected

signals received by several detectors. Our defect detection tool had a minimum size of detection of ~ 0.1 μm in the lateral direction. For the CMP experiments, pre-CMP defect wafer maps were subtracted from post-CMP wafer maps in order to determine the defect adders. Then the wafers were characterized for scratching by means of optical technique.

28. Z.L.W. thanks the NSF (DMR 9733160), the NASA Vehicle Systems Program and Department of Defense Research and Engineering, and the Defense Advanced Research Projects Agency for support. D.C.S. thanks the Cambridge-Cranfield High Performance Computing Facility, Engineering and Physical Science Research Council (GR/S48431/01, GR/S48448/01, and GR/S84415/01) for support.

Supporting Online Material
www.sciencemag.org/cgi/content/full/312/5779/1504/DC1
Figs. S1 to S9
Table S1

3 February 2006; accepted 10 April 2006
10.1126/science.1125767

Regenerative Adsorption and Removal of H_2S from Hot Fuel Gas Streams by Rare Earth Oxides

Maria Flytzani-Stephanopoulos,* Mann Sakbodin, Zheng Wang

Sorbent materials that allow for high-temperature, regenerative desulfurization of fuel gas streams for the anode of a solid oxide fuel cell have been developed. Reversible adsorption of H_2S on cerium and lanthanum oxide surfaces is demonstrated over many cycles at temperatures as high as 800°C, on both fresh or presulfided sorbents, and at very high space velocities. The adsorption and desorption processes are very fast, and removal of H_2S to sub–parts per million levels is achieved at very short (millisecond) contact times. Any type of sulfur-free gas, including water vapor, can be used to regenerate the sorbent surface. Preferably, the anode off-gas stream is used to sweep the desorbed H_2S to a burner.

Conversion of heavy fuels to a hydrogen-rich gas mixture to power solid oxide fuel cells (SOFC) is a cleaner and more efficient way to generate energy than the direct combustion of the fuel, but heavy liquid fuels and coal contain organosulfur compounds that are difficult and expensive to fully remove before fuel reformation. Critical developments will include sulfur-resistant catalysts for the reformers as well as sulfur sorbents that can be regenerated and that operate at temperatures in the range of 650° to 800°C without any performance degradation. Installed upstream of the SOFC anode, the sorbent will protect the nickel-based anode material from sulfurization, which causes irreversible fuel cell power losses.

Sorbents that can be used at SOFC temperatures regenerate poorly, which is a serious drawback that has plagued each of the single- or mixed-oxide combinations that has been considered for hot fuel gas desulfurization. Because of the deterioration of the sorbent structure over time, none of the proposed sorbent materials has become commercially viable (*1*).

The rare earth oxides, especially lanthanum and Ce(III) oxides, have excellent sulfidation thermodynamics in realistic reformate gas compositions, such as the ones produced by steam reforming, autothermal reforming, or partial oxidation of heavy oils, diesel, jet fuels, or by coal gasification (*1–4*). However, if bulk or deep sulfidation of the sorbent is allowed to proceed, the cyclic performance is quickly degraded because of complexities in regeneration, most notably structural changes occurring during the transformation of the sulfided sorbent back to the oxide phase (*5–13*).

We report on a different approach to this problem: We used only the surface of the sorbent in sulfidation and regenerated only the surface of the sorbent upon saturation. By using very high space velocities or short contact times of the gas with the sorbent in regeneration (*14*), bulk regeneration of the sorbent with its attendant structural complexities is prevented. An added benefit of this approach is a very small footprint of the sorber and regenerator units, which is highly desirable for small-scale applications of fuel cells, such as those used in confined locations and for auxiliary power units.

Figure 1A shows the changes in H_2S concentration for the cyclic sulfidation-regeneration of presulfided lanthanum oxide sorbent particles (<53 μm) loaded in a packed-bed reactor run isothermally at 800°C and at a gas hourly space velocity of 400,000 $hour^{-1}$ at standard temperature and pressure (STP). An expanded view of the H_2S concentration profile in one cycle of sulfidation/regeneration is shown in Fig. 1B. The sorbent had a surface area (±SD) of 3.5 ± 0.6 m^2/g at the test conditions (Table 1). The gas mixture composition was chosen to simulate the exit gas stream of a catalytic partial oxidation reformer of a heavy fuel oil, such as JP-8. An exaggerated amount of H_2S (0.1 volume %) was used to shorten the length of each cycle. The carrier gas was He rather than N_2, but this did not affect the results. We also found that substituting H_2 and H_2O, respectively, for CO and CO_2 in the fuel gas had no effect on the adsorption efficiency and sulfur capacity of the sorbent.

Regeneration was conducted in the same fuel gas mixture by switching off the H_2S feed gas. Other gas mixtures can be used to regenerate the sorbent surface equally efficiently (*14*, *15*). The breakthrough time at 1 part per million (ppm) H_2S was the same for all 15 cycles shown in Fig. 1C. The surface sulfur capacity at breakthrough of 1 ppm of H_2S was 0.9 mg sulfur per gram sorbent ($S/g_{sorbent}$). Thus, lanthanum oxide can be used to

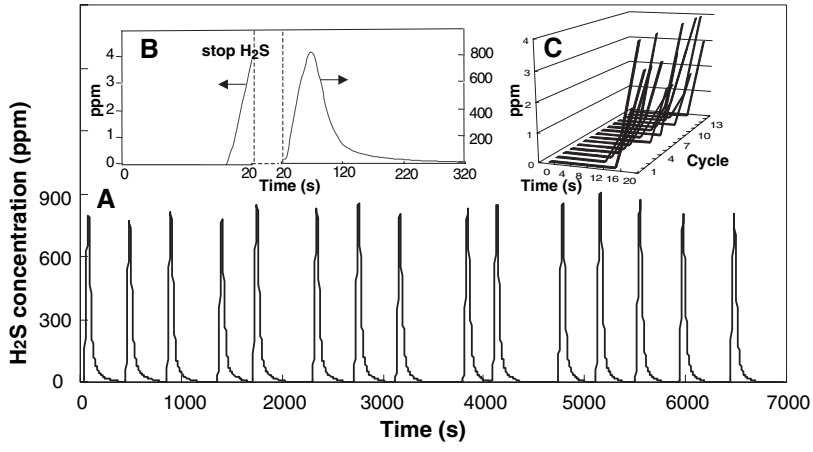

Fig. 1. (**A**) Consecutive sulfidation and regeneration of presulfided La_2O_3 in a packed-bed reactor with the use of simulated reformate gas at 800°C. Switch to desorption at 4 parts per million by volume (ppmv) H_2S. Sulfidation: 0.1% H_2S–20% H_2–20% CO–1% CO_2–10% H_2O–He, space velocity = 400,000 $hour^{-1}$. Regeneration: 20% H_2–20% CO–1% CO_2–10% H_2O–He, space velocity = 400,000 $hour^{-1}$. (**B**) Expanded view of the H_2S concentration profile in one cycle of sulfidation and regeneration of presulfided La_2O_3. (**C**) H_2S breakthrough curves in successive sulfidation cycles of presulfided La_2O_3.

Department of Chemical and Biological Engineering, Tufts University, Medford, MA 02155, USA.

*To whom correspondence should be addressed. E-mail: maria.flytzani-stephanopoulos@tufts.edu